



Formation of a CoMn-Layered Double Hydroxide/Graphite Supercapacitor by a Single Electrochemical Step

Atanu Roy,^[a] Theresa Schoetz,^[b] Leo W. Gordon,^[c] Hung-Ju Yen,^[d] Qingli Hao,^[e] and Daniel Mandler^{*[a]}

Hybrid electric storage systems that combine capacitive and faradaic materials need to be well designed to benefit from the advantages of batteries and supercapacitors. The ultimate capacitive material is graphite (GR), yet high capacitance is usually not achieved due to restacking of its sheets. Therefore, an appealing approach to achieve high power and energy systems is to embed a faradaic 2D material in between the graphite sheets. Here, a simple one-step approach was developed, whereby a faradaic material [layered double hydroxide (LDH)] was electrochemically formed inside electrochemically exfoliated graphite. Specifically, GR was exfoliated under negative potentials by Co^{II} and, in the presence of Mn^{II}, formed GR-CoMn-LDH, which exhibited a high areal capacitance and energy density. The high areal capacitance was attributed

to the exfoliation of the graphite at very negative potentials to form a 3D foam-like structure driven by hydrogen evolution as well as the deposition of CoMn-LDH due to hydroxide ion generation inside the GR sheets. The ratio between the Co^{II} and Mn^{II} in the CoMn-LDH was optimized and analyzed, and the electrochemical performance was studied. Analysis of a cross-section of the GR-CoMn-LDH confirmed the deposition of LDH inside the GR layers. The areal capacitance of the electrode was 186 mF cm⁻² at a scan rate of 2 mV s⁻¹. Finally, an asymmetric supercapacitor was assembled with GR-CoMn-LDH and exfoliated graphite as the positive and negative electrodes, respectively, yielding an energy density of 96.1 μWh cm⁻³ and a power density of 5 mW cm⁻³.

Introduction

The rapid development in portable electronic devices (PEDs), whether smartphones, laptops, wearable electronics, or drones, relies on efficient electrical energy storage (EES) devices. EES for PEDs must have high specific energy and power (performance per electrode mass) as well as energy and power density (performance per electrode volume), rapid charging rates, high safety, and low cost.^[1] Supercapacitors or electrochemical capacitors are EES devices, where the mechanism of electric storage involves the physical separation of charge using electrodes with large surface areas. Supercapacitors have already reached the market and are used in fast charging of public transportation, as well as in combination with fuel cells for maximized energy storage and rapid charging capabilities.^[2]

The two prominent advantages of supercapacitors are high power, which is expressed in fast charging and discharging, and high cyclability.^[3]

Despite their fast charging and high-power features, the relatively low specific energy (1–15 Wh kg⁻¹) and energy density (5–30 Wh L⁻¹) of supercapacitors restrict them as EES devices for most PEDs that require a large and continuous energy supply.^[4] Therefore, the utmost challenge in supercapacitor research is to improve substantially their specific energy and energy density. Supercapacitors are usually made of carbonaceous materials where energy storage depends primarily on the surface area. Although the capacitance of these materials (and therefore, their energy) can be increased by doping, controlling the porosity, and other approaches, in most cases the achieved capacitance does not get close to the theoretical specific


[a] Dr. A. Roy, Prof. D. Mandler
Institute of Chemistry
The Hebrew University of Jerusalem
Jerusalem, 9190401 (Israel)
E-mail: daniel.mandler@mail.huji.ac.il


[b] Dr. T. Schoetz
Department of Chemical Engineering,
The City College of New York
CUNY, New York, NY 10031 (USA)


[c] L. W. Gordon
Department of Chemical Engineering
The City College of New York
CUNY, New York, NY 10031 (USA)

[d] Dr. H.-J. Yen
Institute of Chemistry
Academia Sinica
Nankang District,
Taipei 11529 (Taiwan)

[e] Prof. Q. Hao
School of Chemical Engineering
Nanjing University of Science and Technology
Nanjing 210094 (P. R. China)

 Supporting information for this article is available on the WWW under <https://doi.org/10.1002/cssc.202201418>

 This publication is part of a collection of papers from contributors to the 7th Ertl Symposium on Catalysis in Electrochemistry (Gwangju, South Korea, October 26–29, 2022). Please visit chemsuschem.org/collections to view all contributions.

 © 2022 The Authors. ChemSusChem published by Wiley-VCH GmbH. This is an open access article under the terms of the Creative Commons Attribution Non-Commercial NoDerivs License, which permits use and distribution in any medium, provided the original work is properly cited, the use is non-commercial and no modifications or adaptations are made.

capacitance of graphene (i.e., 550 Fg^{-1}).^[5,6] Thus, to substantially increase the energy of supercapacitors it is intuitive to combine them with compatible faradaic materials. The latter can be subdivided into diffusion-limited (battery type) or non-diffusion limited (pseudocapacitive type) materials.^[7]

Here, we propose coupling between conductive graphite sheets and a layered faradaic material by an original one-step electrochemical process, which combines top-down and bottom-up approaches. Top-down and bottom-up approaches have been reported for assembling EES systems.^[8] Recently, we have shown that electrodes for energy storage can be formed in a single step by either electrochemical or electrophoretic deposition of both the capacitive and the faradaic materials.^[9] Yet, we have never shown that layered faradaic materials can be incorporated efficiently in between graphite sheets using the same approach.

We focus on faradaic 2D materials, specifically, layered double hydroxides (LDHs) of transition metals, with the general structure of $\text{M}_{1-x}^{2+}\text{N}_x^{3+}(\text{OH})_2\text{A}_{x/n}^n$, where M and N are transition metals and A is a counter anion, such as halide or carbonate.^[10] This layered structure and the large *d*-spacing of LDHs allow electrolyte ions to interact with a high number of exposed electrochemically active sites. LDHs exhibit very good ion-exchange and transport properties, and therefore have been studied for EES.^[11] Moreover, LDHs undergo minimal crystal structure changes during the redox reactions, which results in higher stability. Different LDHs have been studied as the positive electrode for supercapacitors such as NiMn-LDH, NiAl-LDH, CoAl-LDH, NiCo-LDH, and CoMn-LDH.^[11–16]

CoMn-LDH has been of particular interest due to its high ionic conductivity (attributed to CoOOH) and the characteristics of $\text{Mn}^{\text{III/VI}}$.^[17,18] It provides good capacitance in an alkaline electrolyte (reported specific capacitance of 1063 Fg^{-1} at a current of 0.7 Ag^{-1}).^[19] Zhao et al. synthesized CoMn-LDH by coprecipitation of Co and Mn on a carbon fiber-based current collector, where the electrode exhibited a specific capacitance of 1079 Fg^{-1} at 2.1 Ag^{-1} . DFT calculations revealed good hybridization of the 3d orbitals of Co and Mn with the 2d orbitals of oxygen, resulting in efficient electron hopping.^[10] Liu et al. highlighted the role of the interlayer spacing of a metal-organic framework templated CoMn-LDH for supercapacitors.^[14] Su et al. reported the hydrothermal synthesis and deposition of CoMn-LDH nanoneedles on a Ni foam current collector for supercapacitors.^[20] In all these aforementioned studies, the electrode materials were deposited on various current collectors, which increased the overall mass and volume, and therefore decreased the specific energy and energy density.

Our approach is to incorporate the LDH inside a graphite current collector (specifically, in between the graphene sheets) to improve the overall electrochemical performance of the hybrid supercapacitor. The performance can be further enhanced through the controlled exfoliation of the graphite, which provides a 3D nanostructure for material deposition.^[21,22] To the best of our knowledge, there are only two reports on NiCo-LDH deposited on partially exfoliated graphite. In their article, Song et al. reported the deposition of NiCo-LDH on partially exfoliated graphite films and also described how this

hybrid system provides a “super highway” for fast electron/ion transport.^[23]

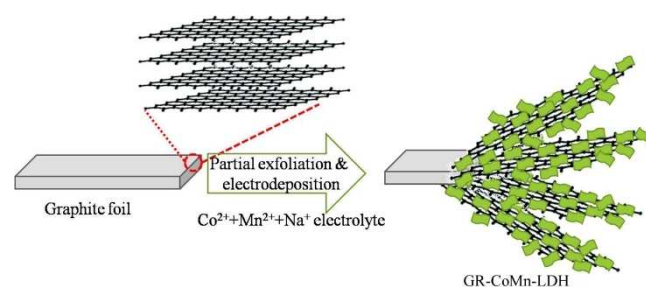
Here, we report on the electrochemical deposition of CoMn-LDH into 3D graphite (GR) by a single step to form GR-CoMn-LDH. This was achieved due to the ability of Co^{2+} to electrochemically exfoliate graphite at negative potentials (see Scheme 1). The nature of exfoliation and LDH deposition was characterized using cross-sectional scanning electron microscopy (SEM) and scanning transmission electron microscopy (STEM). The as-prepared hybrid electrode, GR-CoMn-LDH, exhibits an areal capacitance of 186 mFcm^{-2} at 2 mVs^{-1} . The hybrid electrode shows 83.2% coulombic efficiency after 10000 charge–discharge cycles. Moreover, an asymmetric supercapacitor (ASC), where one electrode is made of the GR-CoMn-LDH whereas the other is composed of the exfoliated graphite, was assembled and showed an areal capacitance of 42 mFcm^{-2} (volumetric capacitance of 233 mFcm^{-3}) along with a good energy density of $96.1 \mu\text{Whcm}^{-3}$.

Results and Discussion

Exfoliation and deposition of the LDH electrode

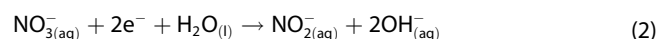
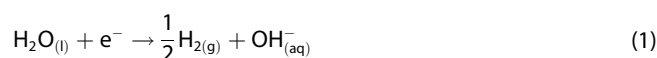
The energy density of graphite electrodes can be improved via metal-ion-driven electrochemical exfoliation, resulting in the deposition of LDHs between its layers. The 2D LDH will contribute to the final capacity and energy density of the graphite electrode through faradaic charge storage. Moreover, these incorporated layered materials can prevent the restacking of the graphene sheets, and thus increase even more capacitive contributions to the current, the cycle life, and the charging rate.^[23,24] Carrying out the whole process in a single step is advantageous as it uses the same material for the exfoliation and deposition, which not only saves time and costs but also enables simpler production and avoids the need to replace the initially intercalating ions with the LDH components. Finally, the potential enables control over both processes (i.e., the exfoliation as well as the LDH deposition) and therefore optimizes the entire process.

The deposition aqueous solution contained $\text{Co}(\text{NO}_3)_2$, $\text{Mn}(\text{NO}_3)_2$, and Na_2SO_4 as the electrolyte. Scanning the potential of the graphite foil (GF) from -5.5 to 0.5 V vs. Ag/AgCl (KCl sat.) and back 6 times resulted in the deposition of CoMn-LDH



Scheme 1. Schematic diagram of the deposited Gr-CoMn-LDH electrode.

(Scheme 1 and Figure S1 in the Supporting Information). The presence of both Na^+ and Co^{2+} drives the cathodic exfoliation of graphite foil through the intercalation of these cations at very negative potentials (< -3 V). The electrochemical exfoliation of graphite in the presence of Co^{2+} has been reported, but by applying positive potentials.^[25] We find that a very negative potential is a prerequisite and the driving force for the exfoliation of the GF. It is evident that at this negative potential the generation of hydrogen also contributes to the exfoliation of the graphite sheets.^[26] This results in the formation of a 3-dimensional (3D) foam-like structure of well-separated graphite layers. The evolution of hydrogen [Eq. (1)], as well as the electrochemical reduction of nitrate [Eq. (2)] to nitrite or other N-species, also generate hydroxyl ions, which cause Co^{2+} and Mn^{2+} to deposit as hydroxides [Eq. (3)]. Thus, the electro-deposition of CoMn-LDHs on graphite foil can be summarized as follows [Eqs. (1)–(3)].^[27]



The negative potential causes the reduction of the metallic ions to the respective metals. Yet, during the reverse scan, the metals are oxidized to their hydroxides at a potential more positive than 0.24 V.^[28]

Elemental composition of the GR-CoMn-LDH electrode

The X-ray diffraction (XRD) patterns of the electrochemically deposited GR-CoMn-LDH samples with the five different Co:Mn compositions (termed CoMn-1:*x*, where *x* = 1, 1.5, 2, 2.5, and 3, see the Experimental Section) is shown in Figure 1a. The XRD patterns of all five materials exhibit the presence of strong graphitic peaks at $2\theta = 26.62$ and 54.73° , which correspond to the (002) and (004) peaks of graphite, respectively.^[29] For CoMn-1:2, the peaks present at $2\theta = 11.6, 36.3, 44.5,$ and 59.6° are due to the (003), (224), (228), and (603) planes of the quintinite group structure of CoMn-LDHs, respectively.^[14] For other samples, these peak positions slightly deviate from their actual place, which suggests the presence of defect levels. In all XRD spectra, there is a wide peak at $2\theta = 19.2^\circ$ ($d = 4.63$ Å), which is attributed to MnO_2 or $\text{Co}(\text{OH})_2$ nanoparticles having a dimension of around 5 nm. In the XRD pattern of CoMn-1:1.5

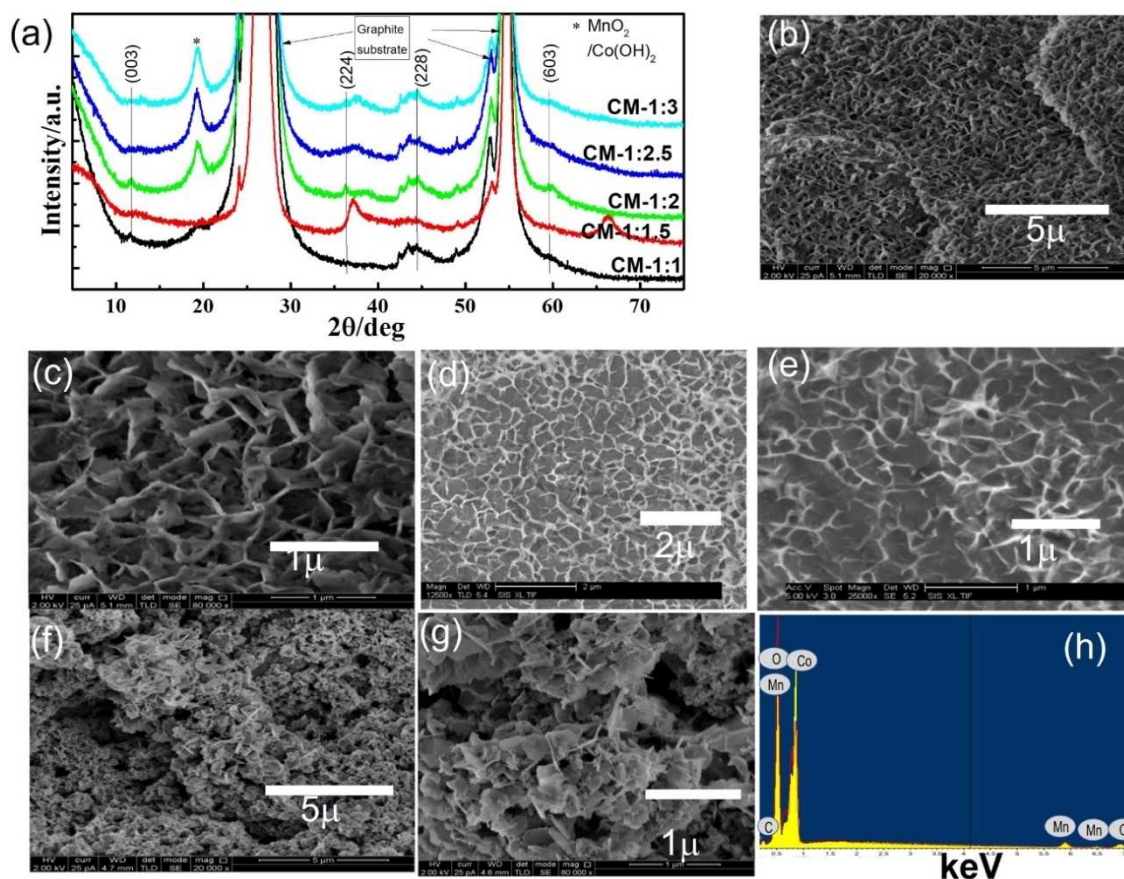


Figure 1. (a) XRD patterns of five CoMn-LDHs. SEM images of (b,c) CoMn-1:1, (d,e) CoMn-1:2, (f,g) CoMn-1:3. A SEM image of bare graphite can be found in Figure S2. (h) EDS spectra of CoMn-2:1.

specifically, a broad peak at $2\theta = 66.2^\circ$ ($d = 1.41 \text{ \AA}$) which may be due to the different phases of MnO_2 , can be seen.

The high-resolution (HR)SEM images of CoMn-1:1 , CoMn-1:2 , and CoMn-1:3 are shown in Figures 1b–g (SEM image of bare graphite is shown in Figure S2). For all three composites, the formation of an opened layered structure on the graphite surface is visible. These types of open layered structures are very promising for energy storage applications as they provide a large exposed surface area for the interaction with the electrolyte ions. In other words, we expect that the materials will have higher capacity and capacitance in comparison with the graphite exfoliated without Co^{II} and Mn^{II} . An energy-dispersive X-ray spectroscopy (EDS) spectrum of CoMn-1:2 is shown in Figure 1h. It clearly depicts the presence of Co, Mn, and O atoms on the surface of the electrode.

The composition of the surface materials, as well as the electronic states of GR-CoMn-LDH, were studied using X-ray photoelectron spectroscopy (XPS). The core-level spectrum of C 1s is shown in Figure 2a. This curve is the convolution of three peaks: the sp^2 -hybridized graphitic carbon (C=C, 284.8 eV), the sp^3 -hybridized carbon–oxygen (C–O, 286.01 eV), and the carbonyl (C=O, 289.41 eV).^[30] The high-resolution deconvoluted spectrum of O 1s is shown in Figure 2b. The peak at 530.3 eV represents the band for hydroxide metal ions in LDH, whereas the peaks at 531.66 and 533.25 eV are due to oxygen bound to carbon or residual water (i.e., O–C/H–O–H bonds).^[31,32] The latter acts as the nucleation center for the formation of metal hydroxides.^[10] Figure 2c represents the high-resolution spectrum of Co 2p, which consists of $\text{Co } 2\text{p}_{3/2}$ and $\text{Co } 2\text{p}_{1/2}$ core levels. The deconvoluted spectrum reveals the presence of Co^{2+} ($2\text{p}_{3/2}$ at 781.64 eV and $2\text{p}_{1/2}$ at 797.36 eV) and Co^{3+} ($2\text{p}_{3/2}$ at 780.31 eV and $2\text{p}_{1/2}$ at 795.24 eV) states. The area associated with the Co^{2+} and Co^{3+} states is 22 and 20% for $2\text{p}_{3/2}$

and 11 and 10% for the $2\text{p}_{1/2}$ peaks, respectively. This indicates that the LDH is composed equally of $\text{Co}(\text{OH})_2$ and $\text{Co}(\text{OH})_3$. There are a few satellite peaks for both $2\text{p}_{3/2}$ and $2\text{p}_{1/2}$ spectra.^[10] The core level deconvoluted spectrum of Mn 2p is shown in Figure 2d, which constitutes $2\text{p}_{3/2}$ and $2\text{p}_{1/2}$. A detailed investigation reveals that these curves consist of Mn^{2+} ($2\text{p}_{3/2}$ at 641.30 eV and $2\text{p}_{1/2}$ at 653.01 eV) Mn^{3+} ($2\text{p}_{3/2}$ at 642.5 eV and $2\text{p}_{1/2}$ at 654.2 eV) as well as Mn^{4+} ($2\text{p}_{3/2}$ at 644.56 eV and $2\text{p}_{1/2}$ at 656.29 eV) states. The spin-orbit separation between $2\text{p}_{3/2}$ and $2\text{p}_{1/2}$ is 11.8 eV, which agrees with other reports and is suitable for energy storage applications.^[33]

The atomic percentage of the different oxidation states of Co and Mn for all five composite electrodes is represented in Table S1, as determined by the XPS measurements. Analyzing the composition of the Co and Mn elements more carefully as a function of the ratio of the elements in the deposition solution reveals the following trends. The total percentage of the Co decreases linearly with decreasing the Co/Mn ratio (Figure S3). Interestingly, while the levels of Co^{II} decrease with decreasing the Co/Mn ratio, the concentration of Co^{III} increases and then decreases (Table S1). Hence, the ratio of $\text{Co}^{\text{II}}/\text{Co}^{\text{III}}$ favors Co^{II} for the low levels of Mn in the electrodeposition solution and then becomes close to unity besides for the CoMn-1:3 where it decreased dramatically. The trend for the Mn is less clear; however, it can be seen that the atomic percentage of Mn^{II} and Mn^{III} increases with decreasing the Co/Mn ratio up to CoMn-1:1.5 , and then it tends to decrease while the atomic percentage of Mn^{IV} is almost constant for all ratios (Table S1). The fraction of Mn^{3+} is the highest for CoMn-1:2.5 while the fraction of Co^{II} is highest for CoMn-1:2 . The ratio of the Co and Mn and their oxidation states will be further discussed alongside the electrochemical performance. However, it is evident that the XPS results confirm the formation of CoMn-LDH, which

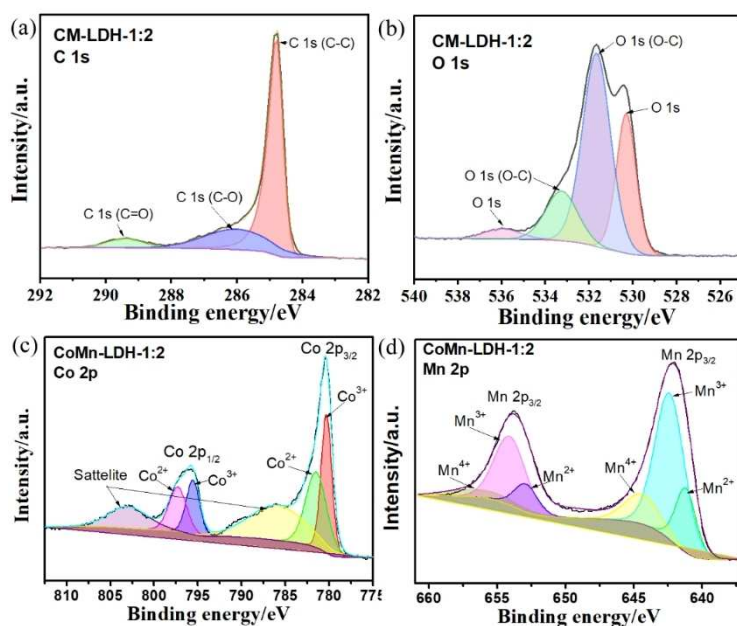


Figure 2. XPS peaks of CoMn-LDH 1:2 showing regions for (a) C 1s, (b) O 1s, (c) Co 2p, and (d) Mn 2p.

is made of multiple oxidation states of Co (Co^{II} and Co^{III}) and Mn (Mn^{II}, Mn^{III}, and Mn^{IV}), which may be beneficial for energy storage through a faradaic process.

Structural characterization of the GR-CoMn-LDH electrode

An important aspect of this electrochemical approach is to confirm the exfoliation and intercalation of the CoMn-LDH inside (i.e., in between the GF sheets) to form GR-CoMn-LDH. This was verified using cross-sectional STEM. The samples were prepared by focused ion beam (FIB), where a thin lamella of CoMn-1:2 was sliced vertically to the electrode surface and analyzed (Figure 3a). A portion of the lamella at a depth of 6 μm from the surface was selected for elemental mapping. The high-angle annular dark-field (HAADF) image of the selected portion is shown in Figure 3b, where the GF sheets can easily be seen. The electrochemical exfoliation is evident by the relatively large spacing of the order of 10 nm, between the GF sheets. The corresponding EDS images for C, Co, Mn, and O are shown in Figures 3c–f, and the corresponding weight and atomic percentage of the elements are presented in Table S2 (for CoMn-1:2). The atomic ratio Mn/Co from EDS (0.75) is substantially lower than that obtained by XPS (1.62, Table S1), indicating that it is indeed the Co²⁺ that drives the exfoliation, and therefore its concentration in the bulk as measured by EDS is higher than that deposited on top of the GR, where the ratio is close to that in the deposition solution. Importantly, the SEM images undoubtedly depict that both Co and Mn are deposited inside the graphite layers. The atomic percentage of oxygen is slightly higher than double the sum of Co and Mn, which suggests the formation of Co_xMn_{1-x}(OH)₂ inside the layers. The penetration of Co and Mn is observable to a depth of around 8 μm , which indicates that the penetration of these ions is even deeper. These cross-sectional images clearly show exfoliated GF as well as deposited CoMn-1:2 LDH. For the deposited CoMn-

LDH to be electrochemically active, the GR-CoMn-LDH must be permeable to ions. The selected area electron diffraction (SEAD) image is shown in Figure 3g, which is typical for an LDH layer. The additional rings in the SEAD pattern may be due to the decomposition of hydroxides by high-energy electrons. Hence, these data imply that in a single electrochemical step, the graphite is exfoliated by the metallic cations that are deposited inside the graphite, at a depth of multiple microns, to form the LDH.

Electrochemical characterization of the GR-CoMn-LDH electrode

The CVs of the five GR-CoMn-LDH electrodes with different Co and Mn ratios recorded in 2.5 M KOH solution are shown in Figure 4a. The high alkalinity is required to stabilize the LDH as well as to facilitate their oxidation (see below). The CVs exhibit nearly rectangular shapes with a redox peak centered between 0.02–0.2 V, depending on the Co/Mn ratio and the scan rate. This indicates that both capacitive as well as faradaic processes play a role in charge storage. Thus, CoMn-LDH and the exfoliated 3D graphite both contribute to the overall performance of the GR-CoMn-LDH electrode. The capacitive contribution of non-exfoliated GR is very low (21 mF cm⁻²). Furthermore, it is evident from the CV that the sample with CoMn-1:2 ratio exhibits the highest current density and thus capacity. We recall that the CoMn-1:1.5 showed the highest total Co and Mn atomic % (Table S1 and Figure S3) and the CoMn-1:2 exhibited the highest percentage of Mn^{III}. Hence, we believe that the best electrochemical performance of CoMn-1:2 is due to the relatively high total percentage of both metals; however, more important is the high fraction of Mn^{III}. It is evident that the capacity increases due to the addition of electroactive faradaic material, which is electrochemically accessed through the GR.

Figure 4b shows the CV of CoMn-1:2 at various scan rates (2–100 mVs⁻¹). Within these scan rates, the areal capacitance varies from 186 to 100 mF cm⁻² for 2 and 100 mVs⁻¹, respectively. The CVs of the other compositions at variable scan rates are shown in Figure S4. The variation of the areal capacitance with scan rates for all five CoMn-composites is shown in Figure S5. From this, it is clear that the areal capacitance of CoMn-1:2 is the highest among all five composites. This shows that the GR-CoMn-LDH electrode combines capacitance (capacitive characteristic) and capacity (faradaic characteristic). The areal capacitance increases with the Mn content up to a Co/Mn ratio of 1:2 (in the deposition solution), and then it decreases. The gradual increase in the overall areal capacitance with the variation of the Co/Mn ratio suggests the ability to fine-tune the cationic composition in LDHs to optimize the total energy storage capability.

The power law (Figure 4c) by which the logarithm of the peak current (*i*) is plotted vs. the logarithm of the scan rate (*v*) is a qualitative approach to analyzing the charge storage mechanism and it discloses the capacitive and faradaic contributions [Eq. (4)].

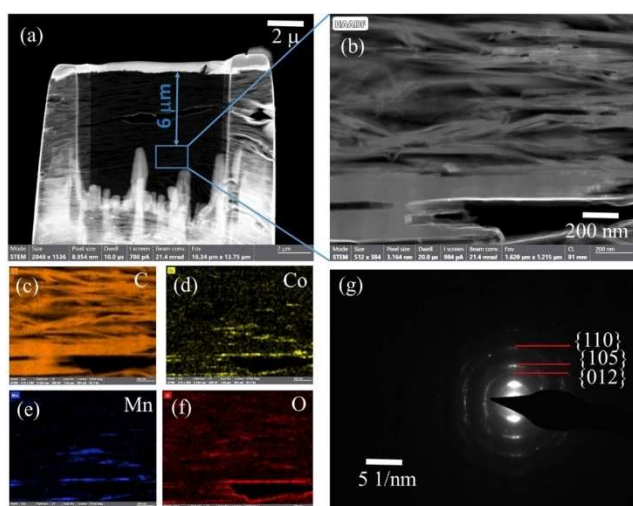


Figure 3. (a) Cross-sectional STEM of CoMn-1:2 obtained by FIB. (b) HAADF image of the cross-section part shown in (a). EDS imaging of the cross-section: (c) C, (d) Co, (e) Mn, and (f) O. (g) SEAD pattern of CoMn-1:2 LDH.

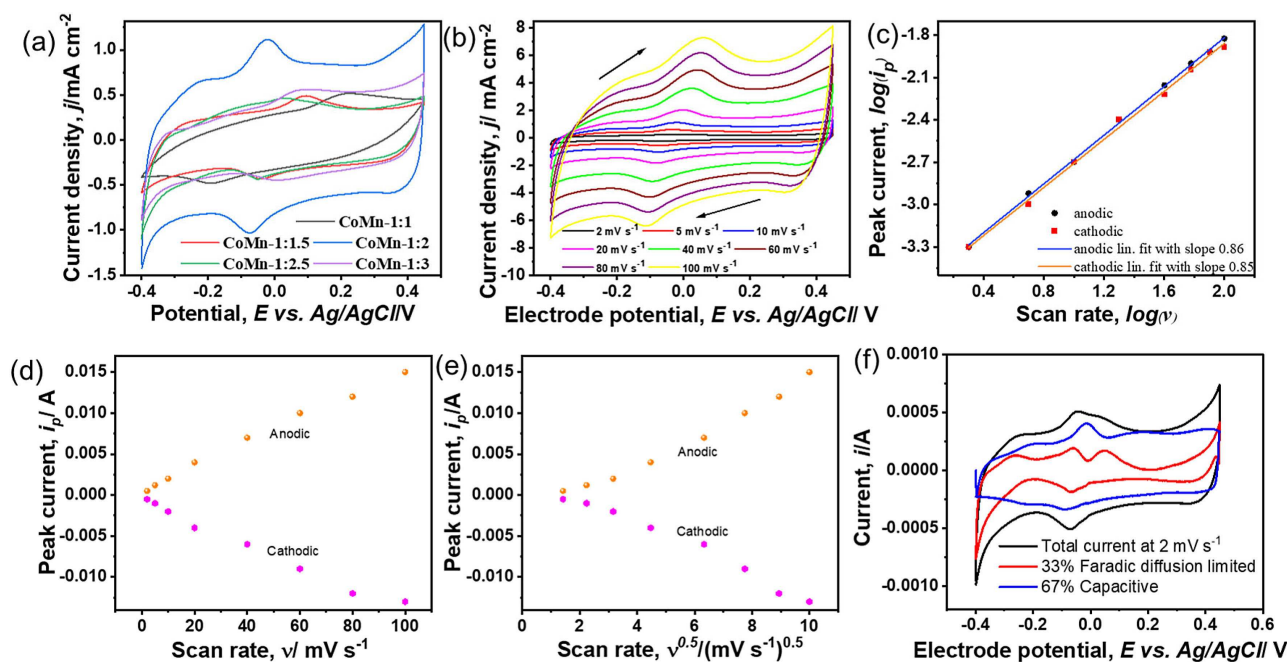


Figure 4. (a) CVs at a scan rate of 10 mV s^{-1} for the five GR-CoMn-LDHs. (b) CV of CoMn-1:2 for different scan rates between 2– 100 mV s^{-1} . (c) Plots of $\log(\text{peak current})$ vs. $\log(\text{scan rate})$. (d) Plots of peak current vs. scan rate. (e) Plots of peak current vs. $(\text{scan rate})^{0.5}$. (f) CV of CoMn-1:2 at a scan rate of 2 mV s^{-1} (black solid lines) along with the contribution due to both faradaic process (red solid line) and capacitive process (blue line).

$$\log i = a \log \sqrt{v} + b \log v \quad (4)$$

For a capacitive mechanism, the slope b of such a plot should ideally be unity, whereas for a faradaic storage mechanism the slope is expected to be 0.5.^[34] The slope of the curve in Figure 4c, which is for the CoMn-1:2 composition, is 0.85 ± 0.01 , indicating a mixed mechanism of capacitive and faradaic processes. This confirms the advantage of our (one-step) approach by which the performance of such a hybrid system can be enhanced by intercalating faradaic-type materials into a highly conductive capacitive material.

We analyzed the other compositions in the same way (Table S3), from which it can be seen that the CoMn-1:2 gives the highest slope, which means that for this specific composition the system exhibits the highest capacitive behavior.

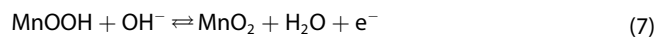
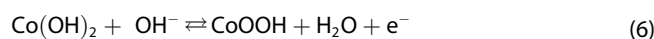
The analysis of variable-rate CV by Wang et al. enables quantifying the (pseudo)capacitive and faradaic diffusion-limited contributions of the different mechanisms to the overall capacity.^[35,36] According to this approach, the current at a particular potential is the sum of both faradaic and (pseudo)capacitive contributions and can be expressed by Equation (5):

$$i(E) = k_1 v^{1/2} + k_2 v \quad (5)$$

where v is the scan rate and k_1 and k_2 are the partial contributions of the faradaic diffusion-limited and capacitive and/or (pseudo)capacitive currents, respectively. We find that k_1 and k_2 for the CoMn-1:2 at the peak potential are 4.64×10^{-3} and 6.17×10^{-2} , respectively. Taking into account that the pseudocapacitive contribution is very low (Figure 4f, blue

curve), implies that k_2 equals the capacitance of the system. The specific capacitance of the CoMn-1:2 is therefore equal to around $200\text{--}300 \text{ F g}^{-1}$ (the electroactive mass is $\approx 0.2\text{--}0.3 \text{ mg}$), which is approximately 50% of the theoretical value of graphene (550 F g^{-1}).

The CV shows that the contribution of the faradaic charge storage is around a third of the total capacity (Figure 4f). This means that the system is predominately characterized by capacitive behavior, which accounts for the charge storage. This relatively high capacitive contribution is presumably the result of the insertion of the LDH into the graphene, which separates the graphene sheets. The faradaic contribution, which is manifested as a pair of cathodic and anodic peaks, is associated with the bimetallic $\text{Co}^{\text{II}}/\text{Co}^{\text{III}}$ and $\text{Mn}^{\text{III}}/\text{Mn}^{\text{IV}}$ redox reaction, which involves also OH^- ions [Eqs. (6) and (7)].^[37] The latter requires that the oxidation will be carried out at a high pH.



The other Co/Mn compositions were also analyzed, and the results are summarized in Table S4 and added to Figure S3. It can be seen that the capacitive contribution (in the percentage of the total capacity) peaks at Co:Mn 1:2 as obtained also from Equation (4). Hence, the best performance correlates well with the highest capacitive contribution; however, clear matching with either the highest total metal content or a specific oxidation state is questionable.

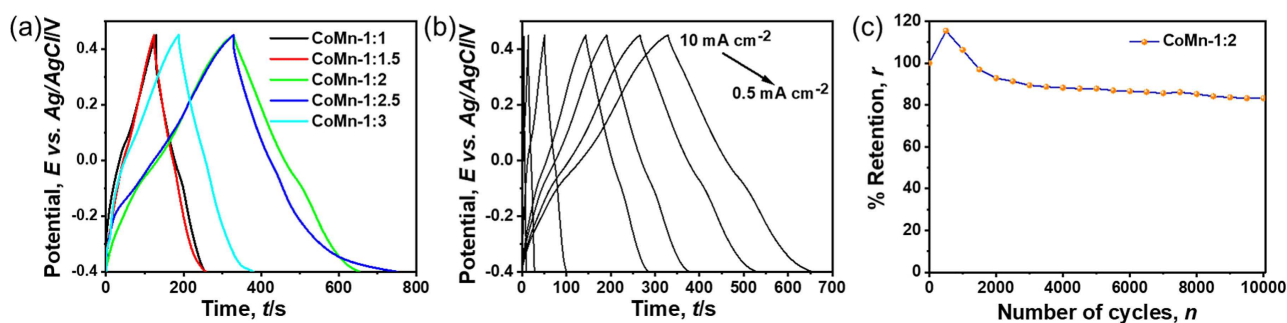


Figure 5. (a) GCD at a current density of 0.5 mA cm^{-2} for all five GR-CoMn-LDH electrodes. (b) GCD of CoMn-1:2 electrode for current densities between 0.5 – 10 mA cm^{-2} . (c) Retention of capacity of the CoMn-1:2 electrode shown via capacity retention over 10000 GCD cycles.

Performance of the GR-CoMn-LDH electrode

The high reversibility of the electrode materials can be confirmed by the coulombic efficiency (Q_{eff} ; Table S5), which is nearly 100% for all scan rates. This means that the insertion and the relevant redox processes of the CoMn-1:2 interface are highly reversible, as mentioned above. The high coulombic efficiency stems from the way the interface was constructed. The intimate contact between the faradaic-type materials and the graphene sheets is the key factor for fast charge transfer and the open structure of the electrochemically exfoliated graphite plays a major role in fast hydroxide diffusion. Figure 5a represents the galvanostatic charge–discharge (GCD) curves of the five GR-CoMn-LDH composite electrodes at a current density of 0.5 mA cm^{-2} . The curves have a close to a triangular shape of a supercapacitor. The GCD curves of the CoMn-1:2 electrode for various current densities (0.5 – 10 mA cm^{-2}) are shown in Figure 5b. The comparative curves for the other composites are shown in Figure S6. The areal capacitance obtained from the GCD data is 191 mF cm^{-2} for a current density of 0.5 mA cm^{-2} [using Eq. (9)], which is relatively high compared to previous studies (see Table S6). This areal capacitance agrees well with the areal capacitance obtained from the CV (i.e., $\approx 186 \text{ mF cm}^{-2}$).

The long charge–discharge cycling (10000 cycles) of the CoMn-1:2 electrode at a current density of 10 mA cm^{-2} is shown in Figure 5c. The electrode exhibits retention of 83.2% of its initial capacity after 10000 GCD cycles, which implies good mechanical and electrochemical stability. The XHR-SEM images of the CoMn-1:2 electrode after 10000 GCD cycles are shown (Figure S7). These images exhibit a slight deviation from the actual shape of the electrode.

To demonstrate its applicability, an asymmetric supercapacitor (ASC), which is composed of two dissimilar electrode materials, was constructed using CoMn-1:2 as the positive electrode and exfoliated graphite as the negative electrode (a schematic diagram is shown in Figure 6a). The negative electrode was fabricated by electrochemical exfoliation of GF in LiClO_4 dissolved in propylene carbonate.^[21,24] The electrochemical performance of exfoliated graphite electrode is presented (Figure S8), and the different performance parameters for ASC are given in Table 1. As the supercapacitor is asymmetric, it is

Current density [mA cm^{-2}]	Areal capacity [mF cm^{-2}]	Energy density [$\mu\text{Wh cm}^{-3}$]	Power density [mW cm^{-3}]
1	38.4	96.1	5
2	31.8	79.4	9.9
4	23.1	57.8	20
6	17.7	44.2	30
8	15.6	38.9	40
10	13.9	35	50.4

expected that the working potential window will be larger than each of the individual electrodes, and its capacity will be higher. Indeed, Figure 6b shows that the CV can be expanded to over 1.5 V, which is significantly larger than each of the electrodes (0.85 V for the CoMn-1:2 and 0.8 V for the exfoliated graphite). The undistorted CV that was extended from 1.2 to 1.8 V suggests that it is possible to operate the ASC within this wide potential window.

The undistorted nature of the CV curves ensures that the hydrogen and oxygen overpotentials are higher for this asymmetric combination and can be attributed to the sluggish kinetics of water reduction and oxidation on graphite. Figure 6c shows the CV curves of the ASC for different scan rates. The ASC exhibits an areal capacitance of 42 mF cm^{-2} (volumetric capacitance 233 mF cm^{-3}) at a scan rate of 2 mV s^{-1} . The performance of the ASC was further investigated by recording the GCD (Figure 6d) within various current densities between 1 and 10 mA cm^{-2} . The ASC exhibits a maximal energy density of $96.1 \mu\text{Wh cm}^{-3}$ at a current density of 1 mA cm^{-2} and the corresponding power density of 5 mW cm^{-3} . The energy density decreases with increasing the current density and reaches a value of around $6.3 \mu\text{Wh cm}^{-3}$ at 10 mA cm^{-2} . The power density increases with increasing the current density and reaches a maximum value of 50.4 mW cm^{-3} at a current density of 10 mA cm^{-2} .

The long-term stability of the ASC was studied by performing 5000 GCD cycles (Figure 6e). It retains 75% of its initial areal capacity after 5000 GCD cycles. It is conceivable that it is the faradaic contribution that is mostly degraded based on the GCD curves.^[38–40] The last few cycles are depicted in Figure 6f. The shape of these GCD curves is similar to that of the initial GCD

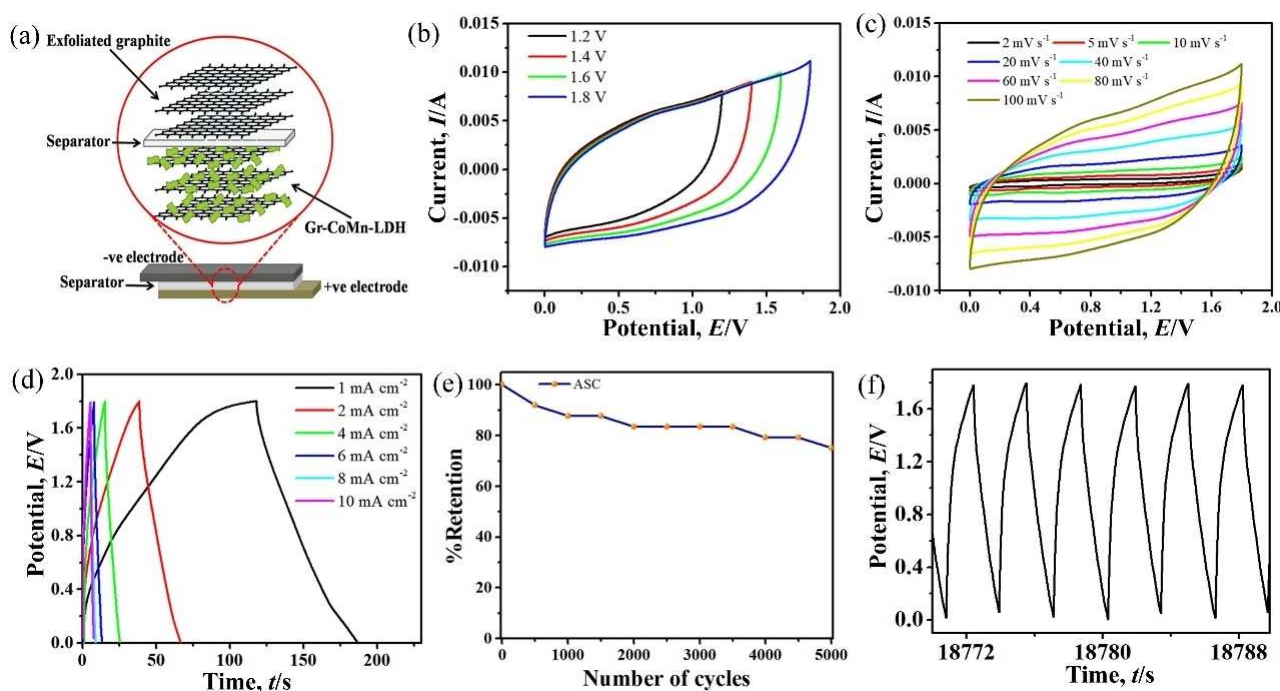


Figure 6. (a) Schematic diagram of the ASC. (b) CV of the ASC at different potential windows, (c) and at different scan rates. (d) GCD of the ASC for different current densities. (e) Stability of the ASC after 5000 cycles. (f) GCD after 5000 cycles.

curves, which confirms the reasonable reversibility and storage capacity of the ASC.

A Ragone plot of the ASC is shown in Figure S9, showing its relatively high energy and power density compared with previous reports. A comparison of energy and power densities of this GR-CoMn-LDH with other reported literature is shown in a tabular form (Table S6). Both the high values of energy and power densities suggest that this material can be an efficient electrode material for a hybrid battery/supercapacitor device.

Conclusions

In an attempt to significantly increase the energy density and maintain the power density of an electric energy storage device, we have assembled a hybrid supercapacitor via a single electrochemical step. Specifically, electrochemistry was used as a means of simultaneously exfoliating graphite and depositing a faradaic-type material, Co–Mn double layered hydroxide (CoMn-LDH), in between the graphene sheets. Two aspects are worth emphasizing: the first comprises the electrochemical one-step exfoliation/deposition. That is, the negative potential applied to the graphite foil in the presence of Co^{II} and Mn^{II} ions caused the exfoliation of the graphite into a 3D foam-like architecture due to hydrogen evolution and the efficient deposition of CoMn-LDH because of the evolved hydroxyl ion. Besides the facile method of preparation, this approach is also responsible for the very good electrochemical performance due to the close proximity of both components, that is, the capacitive graphite/graphene and the faradaic material, CoMn-

LDH. The resulting GR-CoMn-LDH electrode makes the bulky current collector unnecessary and replaces it with an active current collector, which takes part in the charge storage as well. Embedding of the CoMn-LDH inside the exfoliated graphite was confirmed by cross-sectional scanning transmission electron microscopy. The LDH penetrated quite deep inside the graphite. The second important aspect relates to the maximum capacity achieved when the ratio of the Co^{II} to the Mn^{II} in the deposition solution was 1:2, which resulted in an approximately a 1:1.6 atomic ratio on the surface of the GR-CoMn-LDH. This ratio gave the best electrochemical performance in terms of capacity, and therefore was further studied. The electrode showed good stability upon charging–discharging cycling and areal capacitance of 191 mF cm^{-2} at a current density of 0.5 mA cm^{-2} . We attribute the highest performance of this specific Co/Mn ratio to two factors: maximum content of the metals in the deposit ($\approx 22\text{--}25\%$) and even more high percentage of Mn in the CoMn-LDH ($\approx 10\%$). It might well be that the Mn, which can exist in three oxidation states (+2, +3, and +4), is the key to this improved capacity.

The fabricated full asymmetric supercapacitor (ASC) cell shows also high energy and power density. The ASC exhibits a maximal energy density of $96.1 \text{ } \mu\text{Wh cm}^{-3}$ at a current density of 1 mA cm^{-2} and a corresponding power density of 5 mW cm^{-3} . The power density increased with increasing the current density and reached a maximum value of $50.4 \text{ } \mu\text{W cm}^{-3}$ at a current density of 10 mA cm^{-2} . Finally, we believe that this combination of electrochemical exfoliation of 2D capacitive materials together with the electrochemical deposition and embedding of

faradaic type materials is a promising approach for bridging between supercapacitors and batteries.

Experimental Section

Materials

Premium-grade natural graphite foil of thickness 0.25 mm was purchased from Mineral Seal Corporation (Tuscon, AZ). Cobalt nitrate hexahydrate, manganese nitrate tetrahydrate, and polyvinyl alcohol (PVA) were obtained from Merck. Sodium sulfate and potassium hydroxides (KOH) were purchased from Bio-lab, Israel. All these materials were used as received. High-purity deionized water (18.3 M Ω cm) was obtained from an EasyPure UV, Barnstead system and used for the preparation of all the aqueous solutions and rinsing of the samples.

Electrode synthesis procedures

Electrodeposition of CoMn-LDH, as well as the electrochemical exfoliation of the as-received graphite foil (GF) was performed in a single step at room temperature. The GFs (2.5 cm \times 1 cm) were cleaned by ultrasonication (Elmasonic P, 80 kHz) for 10 min each in ethanol, acetone, and high-purity water, respectively. Electrodeposition was carried out in an aqueous solution consisting of 10 mM of Co(NO₃)₂, 10 mM of Na₂SO₄, and different concentrations of Mn(NO₃)₂. The molar ratio between the Co²⁺ and Mn²⁺ (abbreviated CoMn) was 1:1, 1:1.5, 1:2, 1:2.5, and 1:3, which means that the Mn²⁺ concentration was 10, 15, 20, 25, and 30 mM, respectively. Graphite electrochemical exfoliation and CoMn-LDH deposition were performed using cyclic voltammetry (CV) by scanning the potential (6 cycles) from -5.5 to 0.5 V vs. Ag/AgCl (sat. KCl) at a scan rate of 20 mVs⁻¹. Applying such negative potential caused the evolution of hydrogen, which was essential to form highly porous GF (see below). Then, the samples were washed thoroughly with an adequate amount of high-purity water and then dried at 60 °C overnight before use.

Material characterization

Surface morphology was studied by HRSEM (FEI Magellan TM 400 L instrument). XRD (Bruker, D8 Advance) with Cu-K α radiation was used to obtain XRD patterns. XPS was performed using Axis Ultra with a monochromatic Al-K α (1486.6 eV) X-ray source. HeliosNano-lab 460F1 Lite (Thermo Fisher Scientific) FIB was used to prepare the thin lamellas for STEM as well as to perform the cross-sectional SEM. Elemental mapping was performed using STEM (Titan G2 60–300, FEI).

Electrochemical measurements

Electrochemical measurements were performed using an electrochemical workstation (CHI 660E) in a conventional three-electrode set up with Pt wire as a counter electrode, Ag/AgCl (sat. KCl) as a reference electrode in 2.5 M KOH electrolyte. All potentials are quoted versus this reference electrode. The CV and GCD experiments were performed within the potential window of -0.40 to 0.45 V. The scan rates for CV and current densities for GCD varied between 2–100 mVs⁻¹ and 0.5–10 mAcm⁻², respectively. Exfoliated and deposited graphites were used as the working electrodes. Only 1 cm \times 1 cm of the electrodes was exposed to the electrolyte whereas the remaining part of the electrode was wrapped with scotch tape as an insulator.

Performance testing

A parallel plate-type ASC was assembled using the CoMn-1:2 electrode with dimensions of 2 cm \times 2 cm as the positive electrode and a 2 cm \times 2 cm electrochemically exfoliated graphite as the negative electrode. Whatman filter paper (glass microfiber filter GF/A, with a pore diameter of 6 μ m) was used as the separator and 0.1 mg mL⁻¹ of PVA and 2.5 M KOH solution were mixed to form the gel electrolyte. A gel is used to prevent a short circuit between the two electrodes that are positioned very close to each other. Both the electrodes and separator were soaked in a gel electrolyte for 1 h and then dried for 4 h at room temperature before assembling the ASC.

The areal capacitance (from both CV and GCD), energy and power densities (from GCD) of the ASC were calculated using the following equations [Eqs. (8)–(11)]. It should be noted that the calculated capacitance takes into account also the faradaic contributions to the current and, therefore, the values are higher than the real capacitance. Correction of the capacitance was introduced in the text by the variable CV rate analysis, which disentangles the faradaic and capacitive contributions. The values obtained by Equations (8)–(11) were used to compare our results with previous studies.

$$C_A [\text{F cm}^{-2}] = \frac{1}{2Av(E_f - E_i)} \int_{V_i}^{V_f} I(V) dV \quad (8)$$

$$C_A [\text{F cm}^{-2}] = \frac{I \times \Delta t}{A(V_f - V_i)} \quad (9)$$

$$E_v [\text{mWh cm}^{-3}] = \frac{I}{Ad} \int V dt \quad (10)$$

$$P_v [\text{mW cm}^{-3}] = \frac{E_v \times 3600}{\Delta t} \quad (11)$$

Where C_A , A , v , and V are the areal capacitance, area of the electrode, scan rate, and voltage, respectively. $\int_{V_i}^{V_f} I(V) dV$ is the area under the CV curves, $(V_f - V_i)$ is the potential window, I is the discharge current, $\int V dt$ is the area under the discharge curve, d is the thickness of the ASC, E_v is the energy density, and P_v is the power density of the device. C_A was calculated from the CV and GCD using Equations (8) and (9), respectively.

Acknowledgements

AR acknowledges the support of the PBC scholarship program. This work was conducted by Nanomaterials for Energy and Energy-Water Nexus (NEW) Programme under Singapore-HUJ Alliance for Research and Enterprise (SHARE) in the Campus for Research Excellence and Technological Enterprise (CREATE) is supported by the National Research Foundation, Prime Minister's Office, Singapore. The project is supported by the Hebrew University of Jerusalem in the frame of a collaboration between the Academia Sinica (Taiwan) and the Center for Nanoscience and Nanotechnology of The Hebrew University and by the Israel National Research Center for Electrochemical Propulsion (INREP). We acknowledge also the partial support of the ISF-CNSF program (3650/21). The Harvey M. Krueger Family Centre for Nanoscience and Nanotechnology of the Hebrew University is acknowledged.

Conflict of Interest

The authors declare no conflict of interest.

Data Availability Statement

The data that support the findings of this study are available from the corresponding author upon reasonable request.

Keywords: electrochemistry · electrodeposition · graphene · layered double hydroxides · supercapacitors

- [1] Y. Liang, C. Zhao, H. Yuan, Y. Chen, W. Zhang, J. Huang, D. Yu, Y. Liu, M. Titirici, Y. Chueh, H. Yu, Q. Zhang, *InfoMat* **2019**, *1*, 6.
- [2] R. Nigam, K. D. Verma, T. Pal, K. K. Kar, *Applications of supercapacitors*, Vol. 302, Springer International Publishing, **2020**.
- [3] Y. Wang, Y. Song, Y. Xia, *Chem. Soc. Rev.* **2016**, *45*, 5925.
- [4] J. Zhao, A. F. Burke, *J. Energy Chem.* **2021**, *59*, 276.
- [5] A. Borenstein, O. Hanna, R. Attias, S. Luski, T. Brousse, D. Aurbach, *J. Mater. Chem. A* **2017**, *5*, 12653.
- [6] N. Hillier, S. Yong, S. Beeby, *Energy Rep.* **2020**, *6*, 148.
- [7] T. Schoetz, L. W. Gordon, S. Ivanov, A. Bund, D. Mandler, R. J. Messinger, *Electrochim. Acta* **2022**, *412*, 140072.
- [8] U. Patil, S. Chan Lee, S. Kulkarni, J. Soo Sohn, M. Sik Nam, S. Han, S. Chan Jun, *Nanoscale* **2015**, *7*, 6999.
- [9] Y. Ouyang, O. Geuli, Q. Hao, D. Mandler, *ACS Appl. Energ. Mater.* **2020**, *3*, 1784.
- [10] J. Zhao, J. Chen, S. Xu, M. Shao, D. Yan, M. Wei, D. G. Evans, X. Duan, *J. Mater. Chem. A* **2013**, *1*, 8836.
- [11] X. Li, D. Du, Y. Zhang, W. Xing, Q. Xue, Z. Yan, *J. Mater. Chem. A* **2017**, *5*, 15460.
- [12] A. L. Yan, X. C. Wang, J. P. Cheng, *Nanomaterials* **2018**, *8*, 1.
- [13] W. Wang, N. Zhang, Z. Shi, Z. Ye, Q. Gao, M. Zhi, Z. Hong, *Chem. Eng. J.* **2018**, *338*, 55.
- [14] X. Liu, L. Zhang, X. Gao, C. Guan, Y. Hu, J. Wang, *ACS Appl. Mater. Interfaces* **2019**, *11*, 23236.
- [15] H. L. Chia, C. C. Mayorga-Martinez, N. Antonatos, Z. Sofer, J. J. Gonzalez-Julian, R. D. Webster, M. Pumera, *Anal. Chem.* **2020**, *92*, 2452.
- [16] M. P. Browne, Z. Sofer, M. Pumera, *Energy Environ. Sci.* **2019**, *12*, 41.
- [17] Y. Guo, S. Zhang, J. Wang, Z. Liu, Y. Liu, *J. Alloys Compd.* **2020**, *832*, 154899.
- [18] A. Tyagi, Y. Myung, K. M. Tripathi, T. Y. Kim, R. K. Gupta, *Electrochim. Acta* **2020**, *334*, 135590.
- [19] A. D. Jagadale, G. Guan, X. Li, X. Du, X. Ma, X. Hao, A. Abudula, *J. Power Sources* **2016**, *306*, 526.
- [20] D. Su, Z. Tang, J. Xie, Z. Bian, J. Zhang, D. Yang, D. Zhang, J. Wang, Y. Liu, A. Yuan, Q. Kong, *Appl. Surf. Sci.* **2019**, *469*, 487.
- [21] Y. Huang, A. Buffa, H. Deng, S. Sarkar, Y. Ouyang, X. Jiao, Q. Hao, D. Mandler, *J. Power Sources* **2019**, *439*, 227046.
- [22] D. Mandal, P. Routh, A. K. Mahato, A. K. Nandi, *J. Mater. Chem. A* **2019**, *7*, 17547.
- [23] Y. Song, X. Cai, X. Xu, X. X. Liu, *J. Mater. Chem. A* **2015**, *3*, 14712.
- [24] X. Cai, Y. Song, Z. Sun, D. Guo, X. X. Liu, *J. Power Sources* **2017**, *365*, 126.
- [25] A. Ejigu, K. Fujisawa, B. F. Spencer, B. Wang, M. Terrones, I. A. Kinloch, R. A. W. Dryfe, *Adv. Funct. Mater.* **2018**, *28*, 1804357.
- [26] M. H. Dalal, C. Y. Lee, G. G. Wallace, *J. Mater. Sci.* **2021**, *56*, 3612.
- [27] M. S. Kolathodi, M. Palei, T. S. Natarajan, *J. Mater. Chem. A* **2015**, *3*, 7513.
- [28] A. Yavuz, P. Yilmaz Erdogan, N. Ozdemir, H. Zengin, G. Zengin, M. Bedir, *J. Mater. Sci. Mater. Electron.* **2019**, *30*, 18413.
- [29] Q. T. Ain, S. H. Haq, A. Alshammari, M. A. Al-Mutlaq, M. N. Anjum, *Beilstein J. Nanotechnol.* **2019**, *10*, 901.
- [30] F. Song, X. Hu, *J. Am. Chem. Soc.* **2014**, *136*, 16481.
- [31] D. Wang, K. Wang, L. Sun, H. Wu, J. Wang, Y. Zhao, L. Yan, Y. Luo, K. Jiang, Q. Li, S. Fan, J. Li, J. Wang, *Carbon N Y* **2018**, *139*, 145.
- [32] A. Roy, A. Ray, S. Saha, M. Ghosh, T. Das, M. Nandi, G. Lal, S. Das, *Int. J. Energy Res.* **2021**, *45*, 16908.
- [33] Z. Yang, J. Gong, C. Tang, W. Zhu, Z. Cheng, J. Jiang, A. Ma, Q. Ding, *J. Mater. Sci. Mater. Electron.* **2017**, *28*, 17533.
- [34] A. Ray, A. Roy, S. Saha, M. Ghosh, S. Roy Chowdhury, T. Maiyalagan, S. K. Bhattacharya, S. Das, *Langmuir* **2019**, *35*, 8257 acs.langmuir.9b00955.
- [35] A. Roy, F. E. Cancino-Gordillo, S. Saha, U. Pal, S. Das, *Int. J. Energy Res.* **2021**, *1*, 14021.
- [36] J. Wang, J. Polleux, J. Lim, B. Dunn, *J. Phys. Chem. C* **2007**, *111*, 14925.
- [37] T. Deng, W. Zhang, O. Arcelus, J. G. Kim, J. Carrasco, S. J. Yoo, W. Zheng, J. Wang, H. Tian, H. Zhang, X. Cui, T. Rojo, *Nat. Commun.* **2017**, *8*, 15194.
- [38] X. Liu, X. Sun, X. Sun, M. Shen, R. Liu, C. Yang, M. Fan, **2021**.
- [39] T. Li, G. H. Li, L. H. Li, L. Liu, Y. Xu, H. Y. Ding, T. Zhang, *ACS Appl. Mater. Interfaces* **2016**, *8*, 2562.
- [40] G. Wang, Z. Jin, W. Zhang, *J. Colloid Interface Sci.* **2020**, *577*, 115.

Manuscript received: July 25, 2022

Revised manuscript received: August 29, 2022

Accepted manuscript online: August 30, 2022

Version of record online: September 21, 2022